nature geoscience

LETTERS

PUBLISHED ONLINE: 19 OCTOBER 2014 | DOI: 10.1038/NGEO2272

A multi-sill magma plumbing system beneath the axis of the East Pacific Rise

Milena Marjanović[1]*, Suzanne M. Carbotte[1], Helene Carton[1], Mladen R. Nedimović[1,2], John C. Mutter[1] and Juan Pablo Canales[3]

Upper oceanic crust at fast- to intermediate-spreading mid-ocean ridges is thought to form from the intrusion and eruption of magma accumulated within a mid-crustal reservoir present beneath the ridge axis[1–3]. However, the mechanisms for formation of the lower crust are debated[4–8]. Observations from pieces of ancient oceanic crust exposed on land — ophiolites — imply that multiple small magma lenses exist throughout the lower crust at mid-ocean ridges and help form the crust[4,6,7], yet seismic data have imaged only a single lens beneath the innermost axial zones of various mid-ocean ridges[1–3]. Here we use high-fidelity seismic data to image the crust beneath the East Pacific Rise. We identify a series of reflections below the axial magma lens that we interpret as magma lenses in the upper part of the lower crust. These reflections are present between 9° 20′ and 9° 57′ N and are located up to 1.5 km below the axial magma lens. From the geometry and amplitude of the reflections in a zone beneath a recent volcanic eruption[9], we infer that magma drained from a lower lens helped replenish the axial magma lens above and, perhaps, contributed to the eruption. Our data indicate that a multi-level complex of magma lenses is present beneath the East Pacific Rise and probably contributes to the formation of both the upper and lower crust.

Seismic studies of fast- and intermediate-spreading mid-ocean ridges (MORs) reveal a crustal magmatic system composed of a narrow (~1 km) axial magma lens (AML) located in the mid-crust above a broader (4–6 km) crystal mush zone with 2–18% distributed melt extending into the lower crust[1–3,10]. Whereas the AML is believed to be the primary magma source body for the dykes and lavas that make up the upper crust, the role of this melt body in the formation of the lower crustal gabbroic section is actively debated. In the 'gabbro glacier' model most crystal growth occurs within the AML, which subsides by ductile flow to form the entire gabbro section[5]. In contrast, in the 'sheeted sill' model, gabbro formation occurs *in situ* throughout the lower oceanic crust in small magma bodies, with the AML being the shallowest of these[6,7]. Although the multiple-sill model better explains observations of the layered gabbro section in ophiolites[4,6,7] and some geochemical characteristics of oceanic basalts[8], evidence for multiple sills has been lacking in seismic reflection studies at MORs. Lenses in the near-axis and off-axis lower crust have been detected[11,12] but magma sills directly beneath the AML have not been reported.

Here, we present multichannel seismic (MCS) data from the northern East Pacific Rise (EPR) that reveal mid-crustal seismic reflectors located below the AML (hereinafter referred to as sub-axial magma lenses or SAML events). A series of multi-source, multi-streamer lines, resulting in up to 24 parallel reflection profiles spaced 37.5 m apart, were collected along the ridge axis from 8° 20′ to 10° 10′ N (Methods). These data were processed as individual two-dimensional (2D) profiles, and collectively as a swath 3D volume. In addition, a series of across-axis lines spanning the ridge axis from ~9° 37′ to 57′ N were acquired for full 3D imaging. The most prominent SAML events are found between latitudes 9° 20′ and 9° 57′ N (Fig. 1 and Supplementary Fig. 1), where they appear as moderately bright discontinuous reflection events at two-way travel times (TWTT) ranging from ~0.05 to 0.3 s below the AML. Below these brightest events, weaker and/or lower-frequency events are present at greater TWTTs, up to 4.6 s (Fig. 1a,b and Supplementary Fig. 1c,e).

Given the TWTT range of the SAML events below the AML, there are several hypotheses that need to be ruled out for the origin of these events before interpretations in terms of real events from reflective horizons in the crust can be made. These include the presence of a P-to-S converted phase from the AML ($P_{AML}S$), as well as returned energy associated with internal multiples, seafloor side scattering, or out-of-plane imaging of the AML or other crustal horizons. Strong converted shear waves reflected from an AML are expected when the melt content within the lens is high and are detected in previous studies using the method of partial-offset stacking[13,14]. Using a similar approach, a prominent $P_{AML}S$ event at TWTTs of ~0.2 s below the AML is observed in our data (Supplementary Figs 2 and 3), as predicted for this converted shear (Methods). This event is distinct from the SAML events in stacking velocity, frequency content, offset range at which it is observed in pre-stack data (Supplementary Fig. 2), and in the TWTT on stacked images.

Of the other, potential sources that could generate arrivals below the AML, simple intrabed and interbed multiples arising from energy reflecting within layer 2A and/or 2B (Supplementary Figs 4 and 5) can also be ruled out for all of the indicated SAMLs (Fig. 1a,b and Supplementary Fig. 1 and Discussion). The SAML events do not show the consistent relationship with the presence and reflection intensity of the AML above. Moreover, source–receiver offsets and travel times of the SAML events are inconsistent with those predicted for simple intrabed or interbed multiples (Supplementary Figs 4–6). Side-scatter arrivals from rough seafloor topography are present in places along our seismic sections, but occur at greater TWTTs (≥4.8 s) than the SAML events (Supplementary Fig. 7). Furthermore, the SAML events are identified in the migrated 3D seismic volumes available for part of our study area ruling out side-echoes from possible out-of-plane AML events (Supplementary Discussion and Fig. 8).

[1]Lamont-Doherty Earth Observatory, Columbia University, Palisades, New York 10964-8000, USA. [2]Department of Earth Sciences, Dalhousie University, Halifax, Nova Scotia B3H 4R2, Canada. [3]Woods Hole Oceanographic Institution, Woods Hole, Massachusetts 02543-1050, USA.
*e-mail: milena@ldeo.columbia.edu

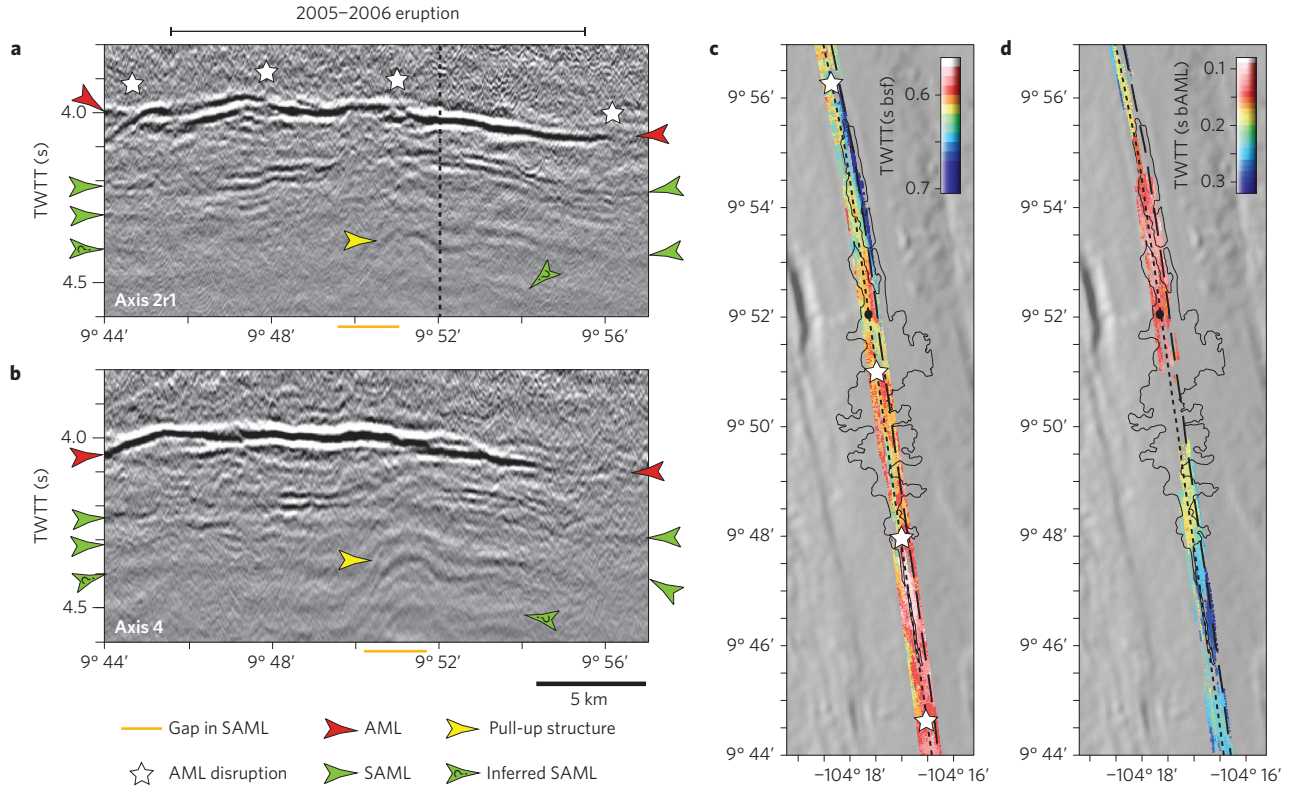

Figure 1 | Characteristics of the AML and SAML seismic reflections imaged along the EPR. a,**b**, Along-axis seismic reflection profiles of axis 2r1 (**a**; dashed line shows location of the gather in Fig. 2) and axis 4 (**b**). **c**,**d**, Map of TWTT to the AML (**c**) and the first SAML reflections below the AML (**d**), both digitized from seismic data, and superimposed on EM300 bathymetry[30] in grey shaded relief. The black line in the map view shows the outline of 2005–2006 lava flow[18]. Dotted and dashed lines show locations of axis 2r1 and axis 4, respectively. The black dot shows the location of the gather in Fig. 2.

On the basis of these considerations, we argue that the SAML events are P-wave reflections from horizons located beneath the AML. Could some of the SAML be previously undetected bottom reflections from a thick magma sill with the AML reflection arising from the top of this body? We consider this possibility unlikely. Using a range of geologically plausible velocities for the region below the AML (~4,000–5,500 m s^{-1}; ref. 10) the estimated depths of the shallowest SAMLs range from ~100 to 800 m (for mapped TWTT ~0.05–0.3 s) beneath the AML implying thick intracrustal sills. Previous waveform modelling of the AML reflection in this region[2,13–15] indicates that the magma lens is not more than 50 m thick, strongly arguing against the above possibility.

If these events are reflections off a magma body similar to the AML, is the material within them molten? The signal-to-noise ratio of the SAML events (even for the brightest ones) is too low for application of a standard amplitude versus offset (AVO) analysis[16]. Hence, to explore the nature of these sub-axial sills, we examine the AVO behaviour of SAML events on common-midpoint (CMP) supergathers using a quasi-forward AVO method[11,16] (Methods). The CMP supergather shows that the AVO response of the SAML event (when normalized) is similar to that of the AML event above it with comparable decrease in amplitude with increasing source–receiver offset (Fig. 2). In addition, the AVO response of the SAML event can be well approximated with simple 1D models calculated for a partially molten sill (with shear velocity within the sill of 800 m s^{-1}, see Methods).

From these analyses, we interpret the SAML events as reflections from thin magma sills similar to the AML, which vary in depth and character along the axis. The SAML events' travel times locate them in the mid-crust, within the upper to mid gabbroic layer (up to 4.6 s, equivalent to 1,200–1,650 m below AML). We speculate that sills at even deeper levels may be present, but high seismic attenuation from melt presence in the overlying crust makes them invisible to our method (attenuation probably accounts for the weak amplitudes and lower frequency of the detected deeper SAMLs). These new seismic images indicate a multi-level, multi-body magma plumbing system beneath the inner axial zone of the EPR, in contrast to previous views of a single, axis-centred mid-crustal melt sill above a broader crystal mush zone[3], and provide direct support for the sheeted sill model for the formation of the crust derived from ophiolite studies (for example, ref. 7).

Within the region of our seismic coverage, two MOR eruptions occurred, in 1991–1992[17] and 2005–2006[9,18], both centred at ~9° 50′ N, providing the opportunity to characterize the multi-sill magma source reservoir beneath the recent eruption (Fig. 1). Seismic data show that the AML is partitioned into three primary segments beneath the eruption, each defined by disruptions in the continuity of the AML reflection that coincide with local deepening of the event or small steps in travel time from one lens segment to the next[19] (Fig. 1). The eruption products above each lens segment show distinct lava chemistry, eruptive volume and dominant flow morphology. The lava morphologies indicative of the highest flow rate and the hottest (high MgO) lavas are both associated with the central lens segment between 9° 48′ and 51.5′ N (refs 20,21). Bright shallow SAML events are present beneath most of the eruption zone and reside at different TWTTs (from ~0.05 to 0.3 s) beneath each AML segment with steps in TWTT of ~0.02–0.05 s from one segment to the next (Fig. 1). These SAML events weaken in reflection amplitude and disappear towards the northern and southern ends of the eruption zone as well as within a region extending ~3,000 m along axis from ~9° 49.9′ to 51.4′ N. This prominent 'gap' in these shallow SAML events is present across the full ~700 m cross-axis width of the swath 3D volume and underlies the northern portion of the central AML segment. Estimates of the

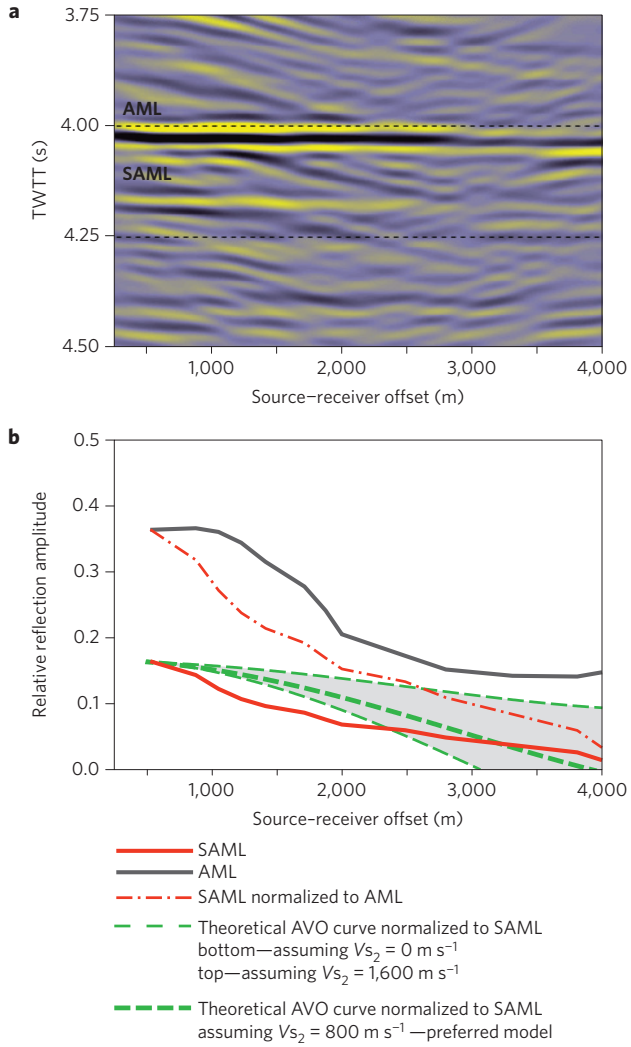

Figure 2 | AVO behaviour of the AML and SAML. a, Normal-move out (NMO)-corrected CMP supergather 19018 (location in Fig. 1) including offsets to 4,000 m. **b**, Filtered AVO response of AML and shallow SAML from the gather shown in **a** (Methods). For comparison, the AVO response of the SAML is also shown normalized to the AML. Theoretical AVO curves, normalized to the AVO response of the SAML are calculated using velocity models with a range of shear velocity within the SAML of $Vs_2 = 0$–1,600 m s^{-1} (grey-shaded area). The theoretical AVO curve with $Vs_2 = 800$ m s^{-1} is shown as the best fit to the AVO response of the SAML event.

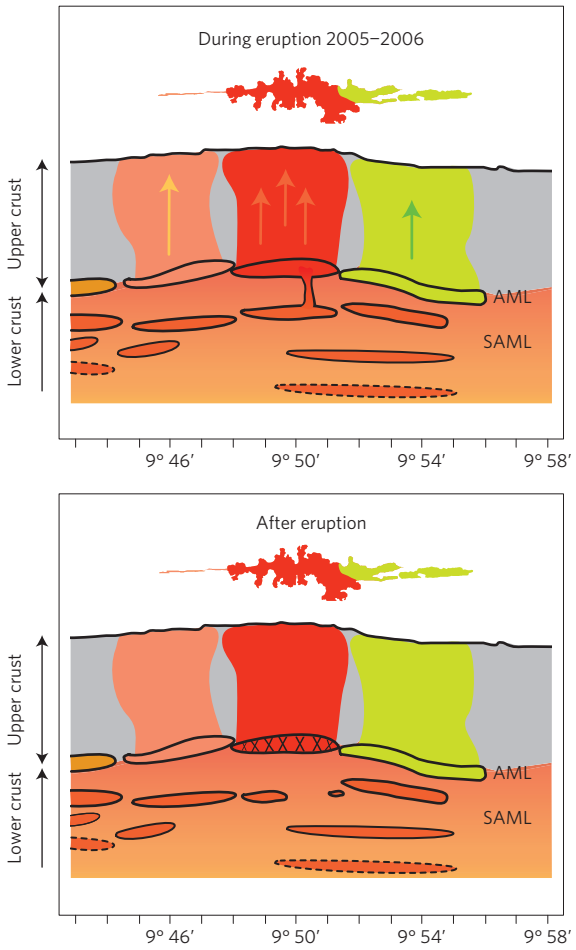

Figure 3 | Scenario for the 2005–2006 eruption. During the eruption, compositionally distinct magmas intruded primarily vertically (arrows) from magma sill segments mapped directly below the eruption site[19,21] (top). After the eruption, the AML and SAML beneath the central eruption site are partially (AML cross-hatched pattern) to fully (SAML gap) crystallized owing to draining of melt during the eruption (bottom). The presence of possible deeper SAMLs is marked by a dashed outline.

melt content of the AML derived from the presence of converted shear arrivals, waveform inversion, and AVO properties indicate, on average, less melt within the AML beneath this central eruption zone than to the north and south[14,22] (Fig. 1). In this same region, below the gap in the shallow SAML, a deeper dome-shaped, low-frequency SAML event (at ~4.33 s TWTT) is observed, which is suggestive of a velocity 'pull-up' due to locally higher velocities in the rocks above (by >50–75 m s^{-1}, Fig. 1), which in this MOR setting could reflect less melt in the overlying crust.

We attribute this local zone of higher crystallinity within the AML, erased reflection signature of the SAML immediately below and locally increased seismic velocities to evacuation of melt from both bodies during the 2005–2006 eruption. In our proposed eruption scenario (Fig. 3), melts drained from a portion of the SAML ascended through the crust, possibly mixing with melts in the overlying central AML segment, and erupted, contributing to the large eruption volumes and high flow rate morphologies observed at the sea floor. Geochemical studies of lavas from both the 1991–1992 and 2005–2006 eruptions lend further support to the interpretation that melts from below the AML contributed to the erupted lavas. Volatile concentrations in olivine melt inclusions from lavas sampled at ~9° 50′ N indicate that the source magmas for both eruptions underwent some crystallization at depths below the AML (ref. 23). Furthermore, geochemical modelling of changes in lava compositions from the 1991–1992 to 2005–2006 eruptions indicate the source magmas for the more recent eruption were derived from the addition and mixing of more evolved melt from deeper in the crust, and not from simple fractional crystallization of the 1991 magma within the AML (ref. 21). Recent studies of subaerial volcanic systems also provide evidence for magma transport from multiple levels within the crust during intrusion and eruption events. From the sequence of seismicity and eruptions observed during the 2010 Eyjafjallajökull eruption in Iceland, it was inferred that draining and depressurization of a shallow magma sill promoted mobilization of magma from deeper sills later in the eruption sequence[24]. In a similar way, during the recent EPR eruptions, withdrawal of magmas from the AML may have led to tapping of melts from the underlying SAML and possibly deeper levels in the crust, contributing melts that differentiated at different depths to mix and erupt during a single eruption episode.

Methods

Seismic survey and data processing. In summer 2008 a multi-streamer (four 6-km-long streamers, each with 468 channels at 12.5 m spacing) and multi-source (two 3,300 cubic inch air-gun arrays) seismic reflection survey was conducted aboard the RV *Marcus G. Langseth* during expedition MGL0812 (ref. 25). One part of the survey was designed to image the axial zone of the EPR in the along-axis direction between 8° 20′ and 10° 10′ N. North of 9° 20′ N, either two or three closely spaced parallel sail lines were acquired over the ridge crest, including lines axis 2r1 (acquired with 7.5 m streamer tow depth) and axis 4 (10 m streamer tow depth; Fig. 1). With the dual source and four-streamer configuration, each sail line yielded eight parallel CMP lines spaced 37.5 m apart with an in-line CMP spacing of 6.25 m. The along-axis lines were processed along their entire lengths assuming a 2D geometry (using streamer 2 and combining shots from both air-gun arrays), and as a 3D-binned swath for the region north of 9° 20′ N where multiple parallel lines were shot[22].

The processing sequence for the 2D sections and swath 3D volumes is similar and includes: trace editing, band-pass filter, spherical divergence correction and amplitude balancing, resampling to 0.004 s (with anti-aliasing filter applied), mute below the first water-bottom multiple, velocity analysis, normal-move out (NMO) correction, stacking and Kirchhoff post-stack time migration. Geometry definition for the swath 3D processing involves identification of separate processing boxes to account for changes in survey line orientation of ~4° and number of CMP lines collected. Data are organized into $37.5 \times 6.25\ m^2$ CMP bins and flexible binning is applied so that each CMP bin contains an equal number of traces corresponding to the nominal fold, here 39. Three-dimensional velocity functions for stacking and migration are constructed by interpolating between velocity functions determined for each 2D section hung from the seafloor bathymetry. Processing is conducted using Paradigm's processing suite Focus[22]. It is important to note that the collected 3D swath is narrower than required to properly migrate and image the AML and SAML events in the cross-axis direction and hence the detailed plan view geometry of these events is not represented in the along-axis data.

In the final seismic sections and volumes, reflected arrivals from the sea floor and AML are imaged, as well as a series of events below the AML that are the focus of this study (Fig. 1 and Supplementary Fig. 1). In addition, refracted arrivals from the steep velocity gradient zone at the base of layer 2A are observed at source–receiver offsets >1,500 m and are stacked to provide an image of the base of layer 2A (ref. 26).

Stacking for $P_{AML}S$. In this study, partial-offset stacking is used to identify S-wave converted phases from the AML ($P_{AML}S$) along line axis 2r1. Pre-stack processing for optimal imaging of the $P_{AML}S$ phase includes band-pass filtering (2–7–20–40 Hz) and application of a dip filter in the f-k domain (dip pass: −0.0009 to 0.002 s/trace) on NMO-corrected (NMO velocity $V = 1{,}520\ m\ s^{-1}$) 24-fold CMP supergathers (Supplementary Fig. 2). After filtering and removing the above NMO, the CMP supergathers are split into single-fold CMP gathers, NMO corrected using $V_{RMS} = 2{,}400\ m\ s^{-1}$, and stacked for source–receiver offsets of 1,500–4,000 m (refs 13,14,27; Supplementary Figs 2 and 3).

AVO analysis. Owing to the low signal-to-noise ratio of the SAML events in the pre-stack data, amplitude variation with offset (AVO) for these events is examined by calculating amplitude envelopes on CMP supergathers. For AVO analysis, we use a 24-fold CMP supergather centred at 19018 CMP with the same processing steps as for imaging the $P_{AML}S$ event (Supplementary Fig. 2). After the initial dip filter described above, we apply a second dip filter with a reject-band between −0.002 and 0.002 s per trace to remove noise arising from shallow crustal events (low velocity) that remains at near-offsets and partially masks the AML and SAML events. We assume that the dip filter has the same effect on both events and its application is considered appropriate. NMO correction ($V = 2{,}600\ m\ s^{-1}$) is applied to the filtered CMP supergather and amplitude envelopes are calculated for the flattened AML and SAML events. Amplitude values are then picked from the amplitude envelopes, smoothed (using simple moving average) and plotted as a function of shot–receiver offset (for offsets from 500 to 4,000 m; Fig. 2).

For comparison, the AVO response for the SAML event is normalized to the AML amplitude at the minimum source–receiver offset. In addition, we calculate a range of theoretical AVO curves and normalize them to the SAML amplitude at the minimum offset. The theoretical curves are calculated using the Zoeppritz equation for reflected P-waves[28] with velocities above the SAML of $Vp_1 = 4{,}500\ m\ s^{-1}$, $Vs_1 = 2{,}600\ m\ s^{-1}$ and within the SAML of $Vp_2 = 2{,}400\ m\ s^{-1}$, and a range of shear velocities within the SAML of $Vs_2 = 0$; 800; and $1{,}600\ m\ s^{-1}$.

Data sources. MCS data are available through the Marine Geoscience Data System (MGDS; www.marine-geo.org/tools/search/entry.php?id=MGL0812). Bathymetric data are from the GMRT Synthesis[29] available through the MGDS. Hydrothermal vent locations are from the Ridge2000 Data Portal of the MGDS at www.marine-geo.org/portals/ridge2000/vents.php?feature_id=EPR. 2005–2006 lava flow outline is from ref. 31 and is available through the MGDS.

Received 2 June 2014; accepted 15 September 2014; published online 19 October 2014

References

1. Detrick, R. S. *et al.* Multi-channel seismic imaging of a crustal magma chamber along the East Pacific Rise. *Nature* **326,** 35–42 (1987).
2. Kent, G. M., Harding, A. J. & Orcutt, J. A. Distribution of magma beneath the East Pacific Rise between the Clipperton transform and the 9° 17′ N Deval from forward modeling of common depth point data. *J. Geophys. Res.* **98,** 13945–13969 (1993).
3. Sinton, J. M. & Detrick, R. S. Mid-ocean ridge magma chambers. *J. Geophys. Res.* **97,** 197–216 (1992).
4. Nicolas, A., Ceuleneer, G., Boudier, F. & Misseri, M. Structural mapping in the Oman ophiolites: Mantle diapirism along an oceanic ridge. *Tectonophysics* **151,** 27–56 (1988).
5. Phipps-Morgan, J. & Chen, Y. J. The genesis of oceanic crust magma injection, hydrothermal cooling, and crustal flow. *J. Geophys. Res.* **98,** 6283–6297 (1993).
6. Boudier, F., Nicolas, A. & Ildefonse, B. Magma chambers in the Oman ophiolite: Fed from the top and the bottom. *Earth Planet. Sci. Lett.* **144,** 239–250 (1996).
7. Kelemen, P. B., Kogu, K. & Shimizu, N. Geochemistry of gabbro sills in the crust–mantle transition zone of the Oman ophiolite: Implications for the origin of the oceanic lower crust. *Earth Planet. Sci. Lett.* **146,** 475–488 (1997).
8. Natland, J. H. & Dick, H. J. B. Formation of the lower ocean crust and the crystallization of gabbroic cumulates at a very slowly spreading ridge. *J. Volcanol. Geotherm. Res.* **110,** 191–233 (2001).
9. Tolstoy, M., Waldhauser, F., Bohnenstiehl, D. R., Weekly, R. T. & Kim, W-Y. Seismic identification of along-axis hydrothermal flow on the East Pacific Rise. *Nature* **451,** 181–184 (2008).
10. Dunn, R. A., Toomey, D. R. & Solomon, S. C. Three-dimensional seismic structure and physical properties of the crust and shallow mantle beneath the East Pacific Rise at 9° 30′ N. *J. Geophys. Res.* **105,** 23537–23555 (2000).
11. Canales, J. P., Nedimović, M. R., Kent, G. M., Carbotte, S. M. & Detrick, R. S. Seismic reflection images of a near-axis melt sill within the lower crust at the Juan de Fuca Ridge. *Nature* **460,** 89–93 (2009).
12. Canales, J. P. *et al.* Network of off-axis melt bodies at the East Pacific Rise. *Nature Geosci.* **5,** 279–283 (2012).
13. Singh, S. C., Kent, G. M., Collier, J. S., Harding, A. J. & Orcutt, J. A. Melt to mush variations in crustal magma properties along the ridge crest at the southern East Pacific Rise. *Nature* **394,** 874–878 (1998).
14. Xu, M. *et al.* Variations in axial magma lens properties along the East Pacific Rise (9° 30′–10° 00′ N) from swath 3D seismic imaging and 1D waveform inversion. *J. Geophys. Res.* **119,** 2721–2744 (2014).
15. Collier, J. S. & Singh, S. C. Detailed structure of the top of the melt body beneath the East Pacific Rise at 9° 40′ N from waveform inversion of seismic reflection data. *J. Geophys. Res.* **102,** 20287–20304 (1997).
16. Nedimović, M. R. *et al.* Frozen melt lenses below the oceanic crust. *Nature* **436,** 1149–1152 (2005).
17. Haymon, R. M. *et al.* Volcanic eruption of the mid-ocean ridge along the East Pacific Rise crest at 9° 45′–52′ N: Direct submersible observations of the seafloor phenomena associated with an eruption event in April, 1991. *Earth Planet. Sci. Lett.* **119,** 85–101 (1993).
18. Soule, S. A., Fornari, D. J., Perfit, M. R. & Rubin, K. H. New insights into mid-ocean ridge volcanic processes from the 2005–2006 eruption of the East Pacific Rise, 9° 46′–9° 56′ N. *Geology* **35,** 1079–1082 (2007).
19. Carbotte, S. M. *et al.* Fine-scale segmentation of the crustal magma reservoir beneath the modern eruptive zone of the East Pacific Rise. *Nature Geosci.* **6,** 866–870 (2013).
20. Fundis, A. T., Soule, S. A., Fornari, D. J. & Perfit, M. R. Paving the seafloor: Volcanic emplacement processes during the 2005–2006 eruptions at the fast spreading East Pacific Rise, 9° 50′ N. *Geochem. Geophys. Geosyst.* **11,** Q08024 (2010).
21. Goss, A. R. *et al.* Geochemistry of lavas from the 2005–2006 eruption at the East Pacific Rise, 9° 46′ N–9° 56′ N: Implications for ridge crest plumbing and decadal changes in magma chamber compositions. *Geochem. Geophys. Geosyst.* **11,** Q05T09 (2010).
22. Marjanović, M. *Signatures of Present and Past Melt Distribution Along Fast and Intermediate Spreading Centers* PhD thesis, Columbia Univ. (2013).
23. Wanless, V. D. & Shaw, A. M. Lower crustal crystallization and melt evolution at mid-ocean ridges. *Nature Geosci.* **5,** 651–655 (2012).
24. Tarasewicz, J., White, R. S., Woods, A. W., Brandsdóttir, B. & Gudmundsson, M. T. Magma mobilization by downward-propagating decompression of the Eyjafjallajökull volcanic plumbing system. *Geophys. Res. Lett.* **39,** L19309 (2012).
25. Mutter, J. C., Carbotte, S. M., Nedimović, N. R., Canales, J. P. & Carton, H. Seismic imaging in three dimensions on the East Pacific Rise. *EOS Trans. Am. Geophys. Union* **90,** 374–375 (2009).

26. Harding, A. J., Kent, G. M. & Orcutt, J. A. A multichannel seismic investigation of upper crustal structure at 9° N on the East Pacific Rise: Implications for crustal accretion. *J. Geophys. Res.* **98,** 13925–13944 (1993).
27. Canales, J. P. *et al.* Seismic evidence for variations in axial magma chamber properties along the southern Juan de Fuca Ridge. *Earth Planet. Sci. Lett.* **246,** 353–366 (2006).
28. Guy, E. D., Radzevicius, S. J. & Conroy, J. P. Computer programs for application of equations describing elastic and electromagnetic wave scattering from planar interfaces. *Comput. Geosci.* **29,** 569–575 (2003).
29. Ryan, W. B. F. *et al.* Global multi-resolution topography synthesis. *Geochem. Geophys. Geosyst.* **10,** Q03014 (2009).
30. White, S. M., Haymon, R. M. & Carbotte, S. M. A new view of ridge segmentation and near-axis volcanism at the East Pacific Rise, 8–12° N, from EM300 multibeam bathymetry. *Geochem. Geophys. Geosyst.* **7,** Q12O05 (2006).
31. Soule, S. A. Interpretation of the extent of the axial summit trough and new lava emplaced during the 2005–2006 eruption(s) at the East Pacific Rise 9° N. (Integrated Earth Data Applications, 2012); http://dx.doi.org/10.1594/IEDA/100071.

Acknowledgements

We thank Captain M. Landow, crew, and technical staff led by R. Steinhaus. We are also very grateful to J. Malloy, D. Foster and C. Mosher from ConocoPhillips for comments and suggestions on the technical part of the paper. This research was supported by NSF awards OCE0327872 to J.C.M. and S.M.C., OCE-0327885 to J.P.C., and OCE0624401 to M.R.N.

Author contributions

All authors participated in the MCS field experiment. M.M. carried out the MCS processing and data analysis. M.M. and S.M.C. interpreted the data and wrote the paper with contributions from all co-authors.

Additional information

Supplementary information is available in the online version of the paper. Reprints and permissions information is available online at www.nature.com/reprints. Correspondence and requests for materials should be addressed to M.M.

Competing financial interests

The authors declare no competing financial interests.